Annals of Biomedical Engineering, Vol. 36, No. 12, December 2008 (© 2008) pp. 2068–2084
DOI: 10.1007/s10439-008-9571-3

Boundary Conditions by Schwarz-Christoffel Mapping in Anatomically Accurate Hemodynamics

EVANGELOS BOUTSIANIS,[1] SUMEET GUPTA,[1] KEVIN BOOMSMA,[2] and DIMOS POULIKAKOS[1]

[1]Laboratory of Thermodynamics in Emerging Technologies, ETH Zurich, ML J 36, 8092 Zurich, Switzerland; and [2]Creare, Inc., Hanover, NH, USA

(*Received 26 September 2007; accepted 18 September 2008; published online 4 October 2008*)

Abstract—Appropriate velocity boundary conditions are a prerequisite in computational hemodynamics. A method for mapping analytical or experimental velocity profiles on anatomically realistic boundary cross-sections is presented. Interpolation is required because the computational and experimental domains are seldom aligned. In the absence of velocity information one alternative is the adaptation of analytical profiles based on volumetric flux constraints. The presented algorithms are based on the Schwarz-Christoffel (S-C) mapping of singly or doubly connected polygons to the unit circle or an annulus with unary external radius. S-C transformations are combined to construct a one-to-one invertible map between the target surface and the measurement domain or the support of the source analytical profile. The proposed technique permits us to segment each space separately and map one onto the other in its entirety. Tests are performed with normal velocity boundary conditions for computational simulations of blood flow in the ascending aorta and cerebrospinal fluid flow in the spinal cavity. Mappings of axisymmetric velocity profiles of the Womersley type through a simply connected circular pipe as well as through a doubly connected circular annulus, and interpolations from *in-vivo* phase-contrast magnetic resonance imaging velocity measurements under instantaneous volumetric flux constraints are considered.

Keywords—Schwarz-Christoffel mapping, Pulsatile flow, Interpolation, Womersley, Annular domain, Hemodynamics.

INTRODUCTION

Atherosclerosis has initiated an ever-expanding interest in arterial flow. Hemodynamics indices based on Wall Shear Stress (WSS)[8] have been proposed and are calculated with the help of Computational Fluid Dynamics (CFD) to pinpoint disease predilection sites. The concurrent development of medical imaging in the last decade has permitted the utilization of increasingly realistic computational domains. Besides anatomical fidelity, there are several prerequisites to render the generated numerical results with sufficient accuracy. Among them, the derivation and imposition of numerically sound and at the same time physiologically relevant boundary conditions are of paramount importance.

The development of computational simulations in anatomically realistic models has been realized in recent years. Several researchers produced numerical investigations of pulsatile blood flow and/or fluid–solid interactions within the arterial tree. Among them are the studies of Jin *et al.*[11] and Shahcheraghi *et al.*[22] in the ascending aorta and the aortic arch. Furthermore, we can refer to fluid–solid interaction simulations within patient-specific cases of abdominal aortic aneurysms.[4,14,28] The coronary arteries present the additional difficulties of embedment onto the moving myocardium and of a continuously bifurcating morphology. Zeng *et al.*[31] studied the effects of cardiac motion on WSS distributions along the right coronary artery. Ramaswamy and co-workers[20] incorporated the combined effects of motion and compliance on WSS along a diseased section of the left anterior descending coronary artery. Boutsianis *et al.*[3] studied the pulsatile blood flow within the first few branches of an anatomically accurate left porcine coronary. In these sample studies, the computational domains were acquired by segmentation and registration of sets of images produced by modern medical imaging modalities, i.e., Magnetic Resonance Imaging (MRI), Computed Tomography (CT), and bi-plane angiography. Hence, the anatomical accuracy is sufficiently accounted for.

The issues of physiological accuracy and/or relevance remain open and depend on appropriate velocity and pressure boundary conditions as in most CFD applications. This is a rather complicated task when approached on a patient specific basis involving technical, ethical, and practical concerns. Modern medical imaging and in particular Phase Contrast MRI

Address correspondence to Dimos Poulikakos, Laboratory of Thermodynamics in Emerging Technologies, ETH Zurich, ML J 36, 8092 Zurich, Switzerland. Electronic mail: dimos.poulikakos@ethz.ch

(PC-MRI)[15,23] has been used successfully to acquire *in-vivo* volumetric flux and/or velocity data. Alternatively, experimental fluid mechanics investigations with solid glass or deformable silicone replicas of realistic arterial geometry have provided another source of information. A characteristic example is given by Perktold *et al.*[18] where Laser Doppler Velocimetry (LDV) measurements are used both for validation of computational results and the determination of inlet boundary conditions. In both approaches, there is the question of transferring these measurements to the computational space. Measurement and computational domains are seldom aligned, e.g., in experimental investigations with deformable models. While anatomical and velocity MRI scans are performed sequentially, the subject's position may change during the process. Discretization errors during segmentation and/or smoothing often result in misalignment of the respective boundary surfaces too. Finally, it is not feasible to acquire MRI velocimetry on every case, especially when another modality is the source of anatomical information, e.g., CT.

Moreover, detailed velocities may not be available at the particular sites of the computational boundary surfaces. In such cases volumetric flux, e.g., acquired with intravascular ultrasound measurements,[12] and/or prescribed mass discharge ratios can be used to produce approximations. It is customary to adapt existing analytical solutions of the respective linearized problem to impose such conditions, like the pulsatile axisymmetric Womersley[29] solutions. Apparently, shape mismatch remains a problem since the targeted computational boundary surfaces do not in general possess the analytical forms defined by the existing analytical solutions. A simple alternative is to extend the computational domain upstream and impose a flat or another ad hoc velocity profile[21] with additional computational cost. The side effects of such an imposed velocity profile depend primarily on the location of this boundary. Even if the computational domain is sufficiently extended to allow for the full development of the flow before reaching the region of interest, artifacts especially in a pulsatile case may still pollute the resulting solution.[21] On the other hand, the influence of this type of errors on targeted quantities of interest, such as WSS distributions, has been shown to be negligible.[17] Other options include the geometrical multiscale[19] approach in which different physical descriptions can be used for the various sections of the computational domain, e.g., the coupling of the full three dimensional Navier Stokes equations with a surrounding one dimensional or lumped parameter model. In this way, the boundaries of the original region of interest become internal interfaces within a larger computational domain. The new boundaries can be strategically located at places where assumptions for the required boundary conditions are easier to make. Migliavacca *et al.*[16] give an excellent example of this technique in a pure application of surgical planning. However, the quantification of realistic parameter values for the one dimensional and/or lumped models is not trivial. Additionally, conservation of mass and momentum must be satisfied across those interfaces. Sophisticated mathematical formulations based on variational methods[2,9] have been proposed for the coupling of one and three dimensional descriptions.

In this study we focus our attention in cases when the imposition of a given velocity profile, either from experimental velocity measurements or by adapting existing analytical solutions, is desirable. We propose an interpolation algorithm based on the Schwarz-Christoffel (S-C) transform[7] to assist the imposition of velocity boundary conditions in the above referenced cases. Conformal mapping of the interior of the unit circle to the interior of any bounded polygon provides a convenient and reversible interpolation function that is used to bridge the gap between simply connected planar surfaces with conforming boundary contours. Apparently, the presented technique has the ability to transfer any axisymmetric analytical profile to the irregular boundary cross-sections that occur in practice. An example application of the proposed algorithm with PC-MRI measurements and the Womersley approximation is presented in a patient-specific case of hemodynamic calculations in the aorta. The S-C map and therefore the proposed algorithm can be easily generalized to doubly connected domains.[10] The motion of the Cerebrospinal Fluid (CSF) in the spinal cavity is an example of pulsatile flow through doubly connected cross-sections, where clinical testing is difficult. CFD investigations[13] are used in conjunction with MRI flow measurements to shed more light on the environment of the CSF system. Similar to the aortic case, we present examples of the adapted algorithm with PC-MRI data and the analytical approximation to pulsatile flow through annular pipes, proposed by Tsangaris.[26]

A strong incentive for the development of the presented interpolation technique is the ability to utilize the same set of boundary conditions, either analytical or measured experimentally, in a 100% repeatable manner on domains of different shape but with identical topology. This approach can facilitate comparisons in the hemodynamics of different patient anatomies or intervention strategies. The rationale for developing computational techniques that allow for the simulation of the vascular hemodynamics of patients lies on the capacity of such tools for predictive diagnostics and simulation based surgical planning.

METHODS

Schwarz-Christoffel Formulas

In its first implementation, the Schwarz-Christoffel formula represented the conformal map from the upper half complex plane to the inner side of any bounded polygon. The method has been extended to include several other domains.[7] In the present work, we need the map from the inner side C of a unit ($R = 1$) circle to the inner surface P of a bounded polygon Γ in the complex space, shown in Fig. 1a. The polygon Γ consists of N vertices, w_k, arranged in counter-clockwise order, is bounded and simply connected. The real interior angles of this polygon are denoted by $\alpha_k\pi$, with $\alpha_k \in (0,2)$. The map is defined by the following equation.

$$f(z) = b + c \cdot \int_{z_0}^{z} \left\{ \prod_{k=1}^{N} \left(1 - \frac{\zeta}{z_k}\right)^{\alpha_k - 1} \right\} \cdot d\zeta, \quad \text{with}$$

$$f(z_k) = w_k, \; k = 1, \ldots, N, \tag{1}$$

where, z_k, denote the pre-vertices upon the unit circle of the polygons' vertices w_k with interior angles $\alpha_k\pi$. b, c, and z_0 are complex constants that need to be determined. The lower integration limit, z_0, is set to zero, for it affects only the value of b. Determining the values of b, c, and the pre-vertices for a given polygon defines the Schwarz-Christoffel parameter problem. The solution of the S-C parameter problem was based on enforcing conditions involving the side lengths of the target polygon Γ, as proposed by Trefethen.[25]

In case of a bounded and doubly connected polygon, $\Gamma_0 U \Gamma_1$ with an inner surface Q, the canonical domain is presented by an annulus A with an outer radius $R = 1$ and an inner radius $\mu < 1$, Fig. 1b. The value μ^{-1} is known as the conformal modulus of Q. The S-C map from A to Q in the complex space is given by Eq. (2).

$$g(z) = b + c \cdot \int_{z_0}^{z} \left\{ \prod_{k=1}^{N} \left[\theta\left(\frac{\zeta}{\mu \cdot z_{0k}}\right) \right]^{\alpha_{0k}-1} \cdot \prod_{m=1}^{M} \left[\theta\left(\frac{\mu \cdot \zeta}{z_{1m}}\right) \right]^{\alpha_{1m}-1} \right\} \cdot d\zeta$$

$$\text{where } \theta(z) = \prod_{d=1,3,5,\ldots}^{\infty} \left(1 - \mu^d \cdot z\right) \cdot \left(1 - \mu^d \cdot z^{-1}\right)$$

$$\text{with} \quad g(z_{0k}) = w_{0k}, \; k = 1, \ldots, N \text{ and}$$

$$g(z_{1m}) = w_{1m}, \; m = 1, \ldots, M, \tag{2}$$

where, z_{0k} and z_{1m}, denote the pre-vertices upon the outer and inner circles of the annulus A of the polygons' vertices, w_{0k} and w_{1m}, respectively. The real interior angles of the polygonal contours are denoted by $\alpha_{0k}\pi$ and $\alpha_{1m}\pi$, with $\alpha_{0k}\pi$ and $\alpha_{1m}\pi \in (0,2)$. Similarly, b, c, and $z_0 \in A$ are complex constants to be determined. Once more b is the image of the base point of the integral in Eq. (2) and therefore $b = g(z_0)$. Determining the correct values of the pre-vertices, the constants b and c and inner radius μ for a given doubly connected polygon defines again an S-C parameter problem. The solution to this problem can be achieved by numerical techniques.[10]

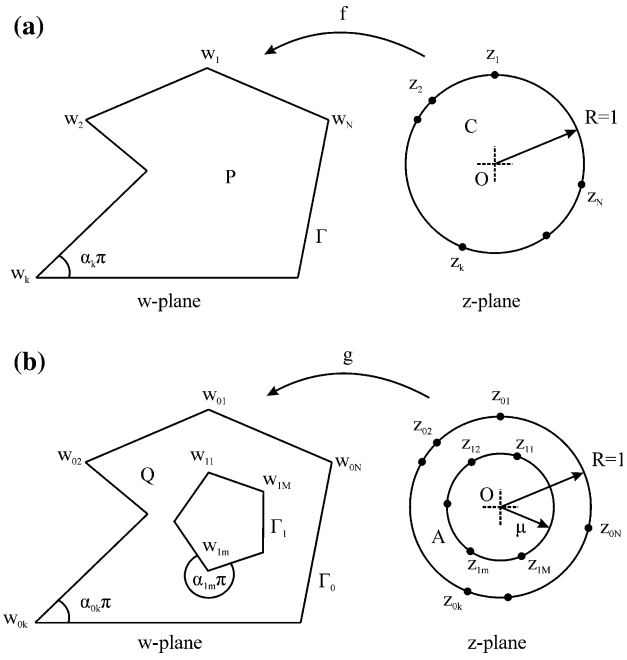

FIGURE 1. Notational convention for the Schwarz-Christoffel transformations: (a) from the inner of a unit circle to the inner of a simply connected polygon and (b) from the inner of a unit annulus to the inner of a doubly connected polygon.

Analytical Velocity Profiles

To demonstrate that Eqs. (1) and (2) provide a convenient way to map analytical velocity profiles to realistic polygonal boundary cross-sections we focused on axisymmetric solutions of the Navier–Stokes equations. To set an example for a simply connected polygon, we refer to the Womersley[29,30] approximation for developed pulsatile flow in a straight circular cylinder under the influence of a known periodic function for the pressure gradient along the cylinder's axis. Womersley showed that by expanding the pressure gradient in Fourier time series one can approximate the time dependent flow rate as the sum of terms obtained for steady and oscillating flows for each component of the expansion. It is useful to invert this solution to the case where the volumetric flow rate is known, as for example in Tsangaris and Stergiopulos.[27] As described by Taylor *et al.*,[24] a Fast Fourier Transform (FFT) can be used to extract the frequency content of a given flux waveform $\dot{Q}(t)$ with fundamental frequency ω.

$$\dot{Q}(t) \approx \sum_{n=0}^{N} B_n \cdot e^{\mathrm{in}\omega t} \quad \text{and} \quad \mathrm{Wo}_n = R_{\mathrm{eq}} \cdot \sqrt{\frac{\omega \cdot n}{\nu}}, \quad (3)$$

where, ν denotes kinematic viscosity and R_{eq} is the circular cylinder's radius. For $n = 1$, Wo_1 is the known Womersley dimensionless number. It quantifies the relative strength between the transient inertial forces and the viscous forces in the fluid. Instantaneous values of axial velocity are then given by the real part of the following sum of Womersley solutions over the N frequencies extracted in Eq. (3) for $r \in [0, R_{\mathrm{eq}}]$.

$$u(r,t) = \frac{2B_0}{\pi R_{\mathrm{eq}}^2} \cdot \left[1 - \left(\frac{r}{R_{\mathrm{eq}}}\right)^2\right] + \mathrm{Real}\left\{\sum_{n=1}^{N}\left\{\frac{B_n}{\pi R_{\mathrm{eq}}^2} \cdot \left[\frac{1 - \frac{J_0\left(\mathrm{Wo}_n \cdot \frac{r}{R_{\mathrm{eq}}} \cdot i^{3/2}\right)}{J_0\left(\mathrm{Wo}_n \cdot i^{3/2}\right)}}{1 - \frac{2 \cdot J_1\left(\mathrm{Wo}_n \cdot i^{3/2}\right)}{\mathrm{Wo}_n \cdot i^{3/2} \cdot J_0\left(\mathrm{Wo}_n \cdot i^{3/2}\right)}}\right]\right\} \cdot e^{\mathrm{in}\omega t}\right\}, \quad (4)$$

where, J_0 and J_1 are Bessel functions of the first kind and of order 0 and 1, respectively.

By adopting the variable change, $y = r/R_{\mathrm{eq}}$, the definition disk of Eq. (4) coincides with the canonical domain of the S-C formula for simply connected polygons. The inverse of map, Eq. (1), can transform any internal point w of the polygonal cross-section P to a complex point $z = f^{-1}(w)$, with $|z| < 1$ and $w \in P$. By setting, $r = |z| \cdot R_{\mathrm{eq}}$, a normal velocity value is then calculated by Eq. (4) for point w.

Caution is needed when considering the area F_P of the target polygonal region P and the area of the circular cylinder where Eq. (4) is defined; termed herein reference domain. It is advantageous to require that both domains have equal areas.

$$R_{\mathrm{eq}} = \sqrt{\frac{F_P}{\pi}} \quad (5)$$

In this way, we can preserve the Womersley number, Eq. (3), between the two domains. The Reynolds number, Rn in Eq. (6), is another important dimensionless parameter quantifying the ratio of the convective inertial forces to the viscous forces that are exerted on the fluid's elements. In unsteady cases, it is common to consider an average Reynolds number, which corresponds to the time-averaged volumetric flux through the investigated cross-section.

$$\mathrm{Rn} = \frac{U_{\mathrm{avg}} \cdot D_{\mathrm{eq}}}{\nu} = \frac{2 \cdot \dot{Q}_{\mathrm{avg}}}{\pi \cdot R_{\mathrm{eq}} \cdot \nu} \quad \text{with} \quad \begin{cases} U_{\mathrm{avg}} = \dfrac{\dot{Q}_{\mathrm{avg}}}{F_P} \\ D_{\mathrm{eq}} = 2 \cdot R_{\mathrm{eq}}, \end{cases} \quad (6)$$

where, D_{eq} is the circular cylinder's diameter and $\dot{Q}_{\mathrm{avg}}$ is the time-averaged value of the required volumetric flux. These two dimensionless numbers characterize the physics of this type of flow. Since our intention is to utilize the analytical solution to provide boundary conditions to another boundary cross-section, it is necessary to maintain equality between these two numbers. It can be seen by Eq. (6) that in order to preserve the Reynolds number it suffices to maintain the prescribed volumetric flow rate in Eq. (3).

The prescribed volumetric flux in Eq. (3) is not maintained *per se*. A correction is needed to ensure conservation of instantaneous flux. In the current investigation, we propose the addition of a constant velocity value, u_{cor}, defined upon P. The normal velocity values should be given by the following sum in conjunction with Eq. (4).

$$u_{\mathrm{tot}}(w,t) = u\left(|z| \cdot R_{\mathrm{eq}}, t\right) + u_{\mathrm{cor}}(t) \quad \text{with} \quad u_{\mathrm{cor}}(t) = \frac{1}{F_P} \cdot \left[\dot{Q}(t) - \iint_P u \cdot dS\right] \quad (7)$$

To present a corresponding case on a doubly connected region we refer to the analytical solution of the axisymmetric linearized Navier–Stokes equations for fully developed pulsatile flow through an annular straight pipe.[26] We generalized this solution to the case where the volumetric flow rate is known, as described in detail in the "Appendix". An FFT can be used to extract the frequency content of a given flux waveform $\dot{Q}(t)$ with fundamental frequency ω.

$$\mathrm{Wo}_n = R_{\mathrm{h}} \cdot \sqrt{\frac{\omega \cdot n}{\nu}} \quad \mathrm{Rn} = \frac{U_{\mathrm{avg}} \cdot R_{\mathrm{h}}}{\nu} \quad \text{with} \quad R_{\mathrm{h}} = 2 \cdot \left(R_{\mathrm{eqo}} - R_{\mathrm{eqi}}\right), \quad (8)$$

where, R_{eqi} and R_{eqo} denote the inner and outer radii, R_{h} the hydraulic diameter and ν the kinematic viscosity. The Womersley number is defined for $n = 1$, Wo_1. The Reynolds number, Rn in Eq. (8), is defined in accordance to Eq. (6) above. Instantaneous values of axial velocity are given by the following summation within the reference domain, $r \in [R_{\mathrm{eqi}}, R_{\mathrm{eqo}}]$.

$$u(r,t) = \frac{2B_0}{k_4} \cdot \left[R_{\mathrm{eqo}}^2 - r^2 + \left(R_{\mathrm{eqo}}^2 - R_{\mathrm{eqi}}^2\right) \cdot \frac{\ln\left(r/R_{\mathrm{eqo}}\right)}{\ln\left(R_{\mathrm{eqo}}/R_{\mathrm{eqi}}\right)}\right] + \mathrm{Real}\left\{\sum_{n=1}^{N}\left[\frac{B_n}{2\pi} \cdot \frac{\left(k_{1n} \cdot K_0\left(i^{1/2} \cdot \mathrm{Wo}_n \cdot \frac{r}{R_{\mathrm{h}}}\right) + k_{2n} \cdot I_0\left(i^{1/2} \cdot \mathrm{Wo}_n \cdot \frac{r}{R_{\mathrm{h}}}\right) - 1\right)}{k_{3n}}\right] \cdot e^{\mathrm{in}\omega t}\right\}, \quad (9)$$

the various constants, k's, are defined in the "Appendix". I_0 and K_0 are the zeroth order modified Bessel functions of the first and second kind.

To maintain equality between the Reynolds and Womersley numbers between the reference and the target polygonal cross-section it suffices to define the radii R_{eqi} and R_{eqo} appropriately. We required that both domains have equal areas by imposing the following definition.

$$R_{eqi} = \sqrt{\frac{A_{in}}{\pi}} \quad R_{eqo} = \sqrt{\frac{A_{out}}{\pi}}, \tag{10}$$

where, A_{in} and A_{out} denote the areas enclosed by the inner and outer contours of the target polygon. By making the variable change, $q = \mu + (1-\mu)/(R_{eqo}-R_{eqi})\cdot(r-R_{eqi})$, the annulus of Eq. (9) coincides with the canonical domain of the S-C transform for doubly connected polygons. The inverse of function (2) maps any internal point w of the polygonal cross-section Q to a complex point $z = g^{-1}(w)$, with $\mu < |z| < 1$ and $w \in Q$. By setting $r = R_{eqi} + (R_{eqo}-R_{eqi})/(1-\mu)\cdot(|z|-\mu)$, a normal velocity value is calculated by Eq. (9) for point w.

Analogously to the simply connected case, area and volumetric flux preservation are sufficient to equalize the Reynolds number. However, the intended volumetric flux, set in Eq. (8), is not maintained in this case too. A correction is proposed below for the normal velocity using formula (9).

$$u_{tot}(w,t) = u\big(|z|\cdot R_{eqo}, t\big) + u_{cor}(t)$$
$$\text{with } u_{cor}(t) = \frac{1}{F_Q}\cdot\left[\dot{Q}(t) - \iint_Q u\cdot dS\right], \tag{11}$$

F_Q, denotes the area of the target polygon Q in this case.

AN ALGORITHM FOR ANALYTICAL VELOCITY PROFILES

In this section we summarize the steps for mapping the analytical velocity profiles described above onto a singly and a doubly connected boundary surface, respectively. In each case, we distinguish among three domains: the target polygon in complex space that represents the given boundary cross-section, the canonical domain of the S-C transform and the reference domain where the analytical normal velocity values are defined. To establish an analogy between the boundary cross-section and the complex plane, this surface cut must be planar. The coordinates of the numerical mesh nodes must be transformed to a local Cartesian system to permit their conversion to complex numbers. Although the origin of this system can be chosen arbitrarily, it is convenient for the calculation of the S-C maps to place it on the centroid of the boundary cross-section. Finally, it is necessary to extract the mesh nodes that form the bounding contour and arrange them in counterclockwise order. These nodes define then the target polygon, P or Q, depicted in Fig. 1. In the algorithm described below, we discern three stages: the initialization stage, the mapping stage and the calculation stage.

Initialization Stage

- FFT of volumetric flux data $(dQ/dt,\omega) \rightarrow B_n$
- Set reference domain R_{eq} by Eq. (5) or (R_{eqi}, R_{eqo}) by Eq. (10)
- Initialize analytical formula $u = u(r,t)$ by Eq. (4) or Eq. (9)

Mapping Stage

- Define target polygon P or Q
- Solve S-C parameter problem $f(z)$ or $g(z)$
- Invert S-C mapping function $f^{-1}(w)$ or $g^{-1}(w)$
- Map nodes to canonical domain $z = f^{-1}(w)$ or $z = g^{-1}(w)$

Calculation Stage

- Initialize velocity values $u(w,t) = u(|z|\cdot R_{eq},t)$ by Eq. (4) or $u(w,t) = u(R_{eqi} + (R_{eqo}-R_{eqi})/(1-\mu)\cdot(|z|-\mu),t)$ by Eq. (9)
- Calculate velocity correction $u_{cor}(t)$ by Eqs. (7) or (11)
- Calculate total velocities $u_{tot}(w,t) = u(|z|\cdot R_{eq},t) + u_{cor}(t)$ or $u_{tot}(w,t) = u(R_{eqi} + (R_{eqo}-R_{eqi})/(1-\mu)\cdot(|z|-\mu),t) + u_{cor}(t)$

In the most general case, the last two stages should be placed within a time loop to allow for cases with moving and/or deforming boundaries.

NON ANALYTICAL VELOCITY PROFILES

We shift to the interpolation of velocimetry data that are available at a mesh of pre-determined points. This is the case of *in-vivo* PC-MRI as well as of other experimental techniques, e.g., LDV. The reference domains are now replaced by the measurement domains, namely M^*_{SC} and M^*_{DC}. Let, M_{SC} and M_{DC}, represent the corresponding bounded regions of interest within the measurement domains for the singly and the doubly connected case. The form of the canonical domains and the target polygons in the complex space, P and Q, remain as before. The link between the target polygon and the measurement space is established by constructing an S-C function for each of these domains, Fig. 2. The required interpolation function, $T_{SC}(w)$,

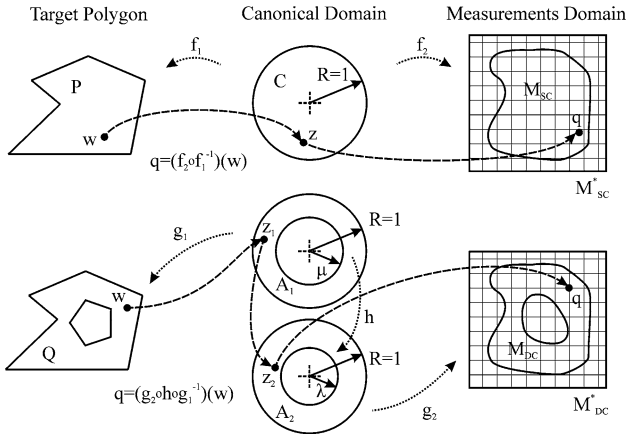

FIGURE 2. Conceptual diagrams of the composite mapping function for the transformation of non-analytical data to a simply connected and a doubly connected polygon.

can be defined by the composition of a direct and an inverse S-C function. The following equation gives an example for the simply connected case.

$$q = T_{\mathrm{SC}}(w) = \left(f_2 \circ f_1^{-1}\right)(w), \text{ with } w \in P \text{ and } q \in M_{\mathrm{SC}}, \tag{12}$$

where f_1 denotes the S-C transform of the unit circle C to P and f_2 the map of C to M_{SC}.

In the doubly connected case, the inner diameter of the canonical domain is among the unknowns of the S-C parameter problem. Therefore, we encounter two unit annuli, A_1 and A_2 with inner diameters μ and λ. Let g_1 denote the map of A_1 to Q and g_2 the map from A_2 to M_{DC}. The interpolating function, $T_{DC}(w)$, is given by Eq. (13).

$$q = T_{\mathrm{DC}}(w) = \left(g_2 \circ h \circ g_1^{-1}\right)(w), \quad \text{with } w \in Q \text{ and } q \in M_{\mathrm{DC}}, \tag{13}$$

the intermediate function, h, is required to connect the canonical domains A_1 and A_2. In this work, h is defined by the following linear transformation for each pair of intermediate points $z_1 \in A_1$ and $z_2 \in A_2$.

$$|z_2| = h(|z_1|) = \lambda + (|z_1| - \mu) \cdot \left(\frac{1-\lambda}{1-\mu}\right), \quad \text{with } \begin{cases} \mu \le |z_1| \le 1 \\ \lambda \le |z_2| \le 1 \end{cases} \text{ and } \arg(z_2) = \arg(z_1), \tag{14}$$

where, $z_1 = g_1(w)$ with $w \in Q$ and $q = g_2^{-1}(z_2)$ with $q \in M_{\mathrm{DC}}$.

The main accomplishment of this process is that we can construct a one to one relation between each point $w \in P$ or Q with a corresponding point $q \in M_{\mathrm{SC}}$ or M_{DC}. We can define an interpolating function within M^*_{SC} or M^*_{DC} without making any provision for the shape of the target boundary cross-section. For example, we could opt for a least-squares surface fit by bicubic B-splines when M^*_{SC} or M^*_{DC} consists of a rectangular grid of points with known normal velocity values, as shown in Eq. (15).

$$u_p(q,t) = u_p((x,y),t) = \sum_{k,l} c_p^{kl}(t) \cdot M_p^k(x) \cdot N_p^l(y), \quad \text{with } \begin{cases} q = x + iy \\ q \in M_p^*, p = \{\mathrm{SC},\ \mathrm{DC}\} \end{cases}, \tag{15}$$

where, c^{kl} represents the interpolation coefficients matrix and $M^k(x)$ and $N^l(y)$ the normalized cubic B-splines for each direction. In the general case of transient velocity fields and/or with a moving underlying grid, the coefficients matrix and the spline knot distributions must be calculated for each time step.

It is noted that the volumetric flux is not preserved between the target polygons and the measurements domains unless they possess identical bounding contours. Whenever we wish to impose the given volumetric flux time history, a simple correction can be applied by Eq. (16).

$$u_{p,\mathrm{tot}}(w,t) = u_p(q,t) + u_{\mathrm{cor}}(t) \quad \text{with } u_{\mathrm{cor}}(t) = \frac{1}{F_D} \cdot \left[\dot{Q}(t) - \iint_D u_p \cdot dS\right] \text{ and } D = \{P, Q\}, p = \{\mathrm{SC},\ \mathrm{DC}\}, \tag{16}$$

where, F_D, denotes the area of the target polygon and $\dot{Q}(t)$ the instantaneous volumetric flux through the corresponding measurements domain.

AN ALGORITHM FOR NON ANALYTICAL VELOCITY PROFILES

The interpolation algorithm for analytical profiles needs to be revamped to facilitate the adaptation of velocimetry data known at a mesh of points. Let us assume that this data refer again to the normal velocity component at a predetermined number of time steps. The main difference is that two S-C maps and a function composition are now necessary. A prerequisite is that both the measurements domains and the boundary cross-sections are planar in order to convert their coordinates to complex numbers. Local Cartesian systems are required for both spaces, while the origins of these systems may again be placed conveniently at the centroids. The canonical domain for the S-C maps in the simply connected case is the unit circle, whereas there are two unit annuli with different inner diameters in the doubly connected case. In addition to the extraction of the nodes that form the

bounding contours of the boundary cross-sections, we must define the surrounding contours of the mesh of measurement nodes to create the second target polygons. The proposed algorithm is divided in the familiar stages: the initialization stage, the mapping stage and the calculation stage.

Initialization Stage

- Construct measurements interpolation $u_p((x,y),t)$, $p = \{\text{SC, DC}\}$, $\forall t$, in Eq. (15)

Mapping Stage

- Define target polygons (P, M_{SC}) or (Q, M_{DC})
- Solve S-C parameter problems ($f_1(z)$, $f_2(z)$) or ($g_1(z_1)$, $g_2(z_2)$)
- Invert S-C mapping function $f_1^{-1}(w)$ or $g_1^{-1}(w)$
- Construct composition function $(f_2 \circ f_1^{-1})(w)$ or $(g_2 \circ h \circ g_1^{-1})(w)$
- Map nodes to measurements domain $q = (f_2 \circ f_1^{-1})(w)$ or $q = (g_2 \circ h \circ g_1^{-1})(w)$

Calculation Stage

- Initialize velocity values $u_p(w,t) = u_p(q,t)$, $p = \{\text{SC, DC}\}$ by Eq. (15)
- Calculate velocity correction $u_{\text{cor}}(t)$ by Eq. (16)
- Calculate total velocities $u_{\text{tot},p}(w,t) = u_p(q,t) + u_{\text{cor}}(t)$, $p = \{\text{SC, DC}\}$

Note that since the measurements are available at all time steps, the "initialization stage" can be performed separately before all the time steps. The inclusion of the mapping stage within the time loop is essential when at least one of two conditions occur. That is when the boundary surface moves and/or deforms or when the region of interest in the measurements domain, M_{SC} or M_{DC}, moves and/or deforms.

EXAMPLE APPLICATIONS

Target Boundary Surfaces and Required Volumetric Flux

The algorithms were checked on two occasions. Blood flow in the ascending aorta is a paradigm of flow through an initially branchless, cylindrical domain with simply connected cross-sections. Conversely, the motion of the cerebrospinal fluid in the spinal cavity is an example of pulsatile flow through a doubly connected channel. MRI imaging was used to extract anatomical data, which were segmented to produce anatomically accurate surface reconstructions for both cases. CFD volumetric meshes were built on top of them after the introduction of planar cuts to permit the imposition of boundary conditions. The "inlets" to these meshes were the targeted boundary cross-sections, Figs. 3a and 3b. The inlet mesh to the ascending aorta is unstructured and consists of 985 quadrilateral faces and 1038 nodes. Its bounding contour has 104 vertices while the cross-sectional area is $6.54 \cdot 10^{-4}\text{m}^2$. A structured quadrilateral grid having 900 faces and 950 nodes meshes the CSF inlet, which has a cross-sectional area of $2.51 \cdot 10^{-4}\text{m}^2$. The inner and outer contours have 50 vertices each. We assumed that the boundary surfaces neither deformed nor moved.

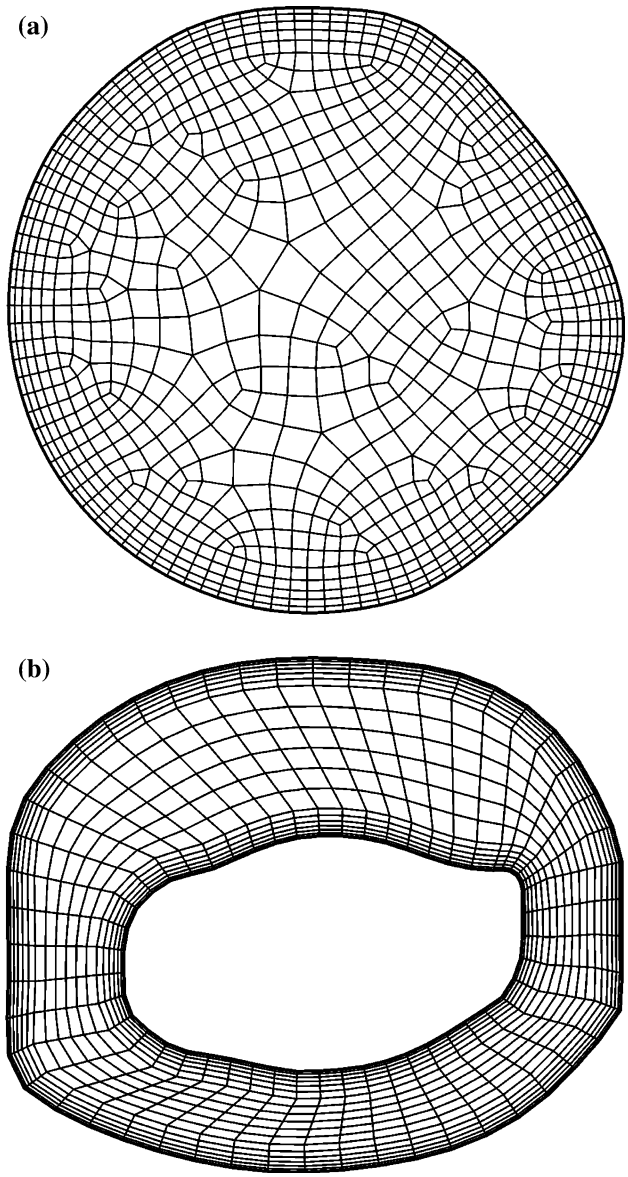

FIGURE 3. Numerical meshes of the target boundary cross-sections: (a) inlet to the ascending aorta and (b) inlet to the spinal cavity at the base of the skull.

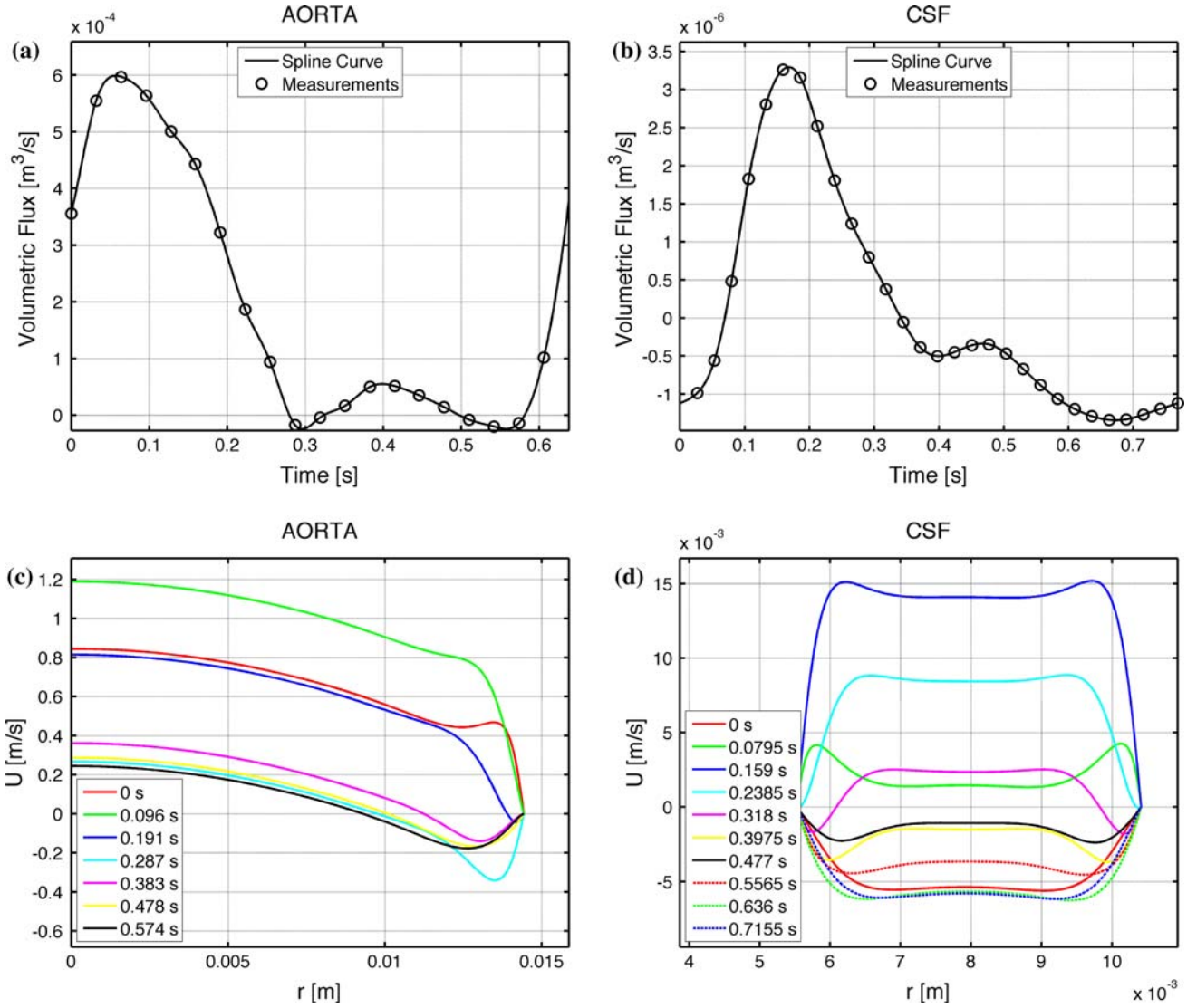

FIGURE 4. Measured volumetric fluxes and the corresponding axisymmetric pulsatile velocity profiles at several time instances through the inlet to the ascending aorta (a, c) and the inlet to the spinal cavity (b, d).

In-vivo PC-MRI volumetric flux data were acquired at geometrical planes with regions of interest that matched with each inlet. The anatomical MRI and PC-MRI scans in the ascending aorta and in the spinal cavity belong to volunteers. The measurements in the ascending aorta, Fig. 4a, revealed increased cardiac output with average volumetric flow of 11.46 L/min. The heart rate was above physiological resting conditions at 94 bpm resulting to a time-period of 0.638 s. The measurements in the spinal cavity were taken at the base of the skull with an average flux rate of 5.8 L/min and time-period of 0.7685 s, Fig. 4b. Our task is to impose the measured instantaneous volumetric fluxes, shown in Figs. 4a and 4b, through the selected boundary cross-sections; firstly by transforming the appropriate analytical velocity profile and secondly by interpolating from the measurements planes.

Maps of Analytical Velocity Profiles

The algorithm results for analytical velocity profiles are presented in this section. For the aortic case, blood was assumed to have a density of 1060 kg/m^3 and constant viscosity of 0.00345 Pa s. At the initialization stage, an FFT transform of the flux history of Fig. 4a produced the required Fourier coefficients with angular frequency 9.8483 s^{-1}. The equivalent radius was calculated as 1.44 cm by Eq. (5). These values result to a Womersley number of 25.1 and an average Reynolds number of 2606. The corresponding axisymmetric velocity profile is shown in Fig. 4c. CSF density and

viscosity were set at 1000.58 kg/m^3 and $6.9161 \cdot 10^{-4}$ Pa s. Similarly, an FFT transform of the flux history of Fig. 4b produced the Fourier coefficients with angular frequency 8.1759 s^{-1}. The equivalent inner and outer radii of the reference annulus were calculated at 0.55 and 1.04 cm according to Eq. (10). The resulting axisymmetric profile is depicted in Fig. 4d at several time instances. It corresponds to a Womersley number of 33 and an average Reynolds number of 8.23, based on a hydraulic diameter of 0.98 cm by Eq. (8).

In the mapping stage, the numerical solution of the S-C parameter problem for the aortic case was obtained with the S-C MATLAB Toolbox (MATLAB Central File Exchange, http://www.mathworks.com/matlabcentral/) by Driscoll.[5,6] The results of the calculation stage are shown in Fig. 5a as carpet plots at three time-steps. The carpet surface is colored by velocity magnitude, while the locations of the faces centers are overlaid as red spheres. A continuous red line at zero velocity, best discerned in the third time-step, denotes the target polygon. The resemblance between the analytical and the mapped velocity profiles is readily apparent. The magnitude of the velocity correction averaged below 5% of the mean instantaneous velocity. The discrepancy intensifies at those time-steps that the velocity profile displays a steep gradient near the wall.

The numerical solution of the S-C parameter problem in the CSF domain was achieved by a software package in FORTRAN 77, called DSCPACK (ACM Digital Library, http://portal.acm.org/).[10] The conformal modulus of the target polygon was $\mu^{-1} = 1.767$. The corresponding set of velocity encoded carpet plots is given in Fig. 5b. The continuous red line contours at zero velocity denote the boundaries of the target polygon. The average velocity correction remained below 4% of the mean instantaneous velocity. A finer mesh in the near wall region would further limit the required corrections in both domains.

Maps of Non Analytical Velocity Profiles

The results of direct interpolation between a measurement plane and a target boundary cross-section are presented in this section. We post-processed the acquired PC-MRI scans and decoded the normal velocity distributions. A non-moving rectangular Cartesian plane formed the measurement domain. The aortic data were acquired at a series of 20 256 × 256 16-bit gray scale images with uniform pixel spacing of 0.938 mm and slice thickness of 4 mm. The CSF series contained 30 512 × 512 16-bit gray scale images with uniform pixel spacing of 0.4 mm and slice thickness of 6 mm. The initialization stage was concluded by constructing a series of least-squares bi-cubic B-spline surface fits with automatic knot sequence, defined by Eq. (15), for each time-step and measurements plane. The MATLAB NAG Foundation Toolbox (nag Numerical Algorithms Group, http://www.nag.co.uk/index.asp) was used for this purpose.

The target polygons in Fig. 3 did not move or deform. The solutions to the S-C parameter problems for the mapping functions, $f_1(z)$ and $g_1(z)$ and their inversions, were identical to those of the previous paragraph. The construction of $f_2(z)$ and $g_2(z)$, needed for the composition mapping functions $(f_2 \circ f_1^{-1})(w)$ and $(g_2 \circ h \circ g_1^{-1})(w)$, required the definition of the bounding polygons M_{SC} and M_{DC}. This is a segmentation problem within M^*_{SC} and M^*_{DC} for each time-step. Specialized software for medical imaging analysis, Amira v3.1 (Mercury Computer Systems SAS, http://www.tgs.com/), was used for this task. The lateral motion of the aortic wall within the measurements plane is significant and the bounding polygonal contour deforms. Separate $f_2(z)$ and $(f_2 \circ f_1^{-1})(w)$ were calculated at each time step. Depictions of $f_1(z)$ and $f_2(z)$ are given in Fig. 6a for the first time step. A series of contour plots showing the evolution in time of the interpolating surface fit, the bounding polygonal contour and the mapped faces centers in the measurement plane is given in Fig. 7a. The same task was performed once for the case of the CSF flow because the region of interest remained unchanged through time within M^*_{DC}. Figure 7b depicts three time instances of the interpolating surface fit, the bounding polygonal contour and the mapped faces centers in the measurements plane of the CSF case. The shape of the interpolated velocity contours reveals the presence of significant noise. The conformal modulus of $g_2(z)$ was $\lambda^{-1} = 1.408$ in this case. It can be seen that the conformal moduli of $g_1(z)$ and $g_2(z)$, $\mu^{-1} = 1.767$ and $\lambda^{-1} = 1.408$, differ significantly. This is caused by the dissimilarity of the inner polygonal contours between the target boundary cross-section and M_{DC} due to segmentation errors and smoothing. The functions $g_1(z)$ and $g_2(z)$ are shown in Fig. 6b. The software tools mentioned in the analytical profile cases were used for the numerical solution of the S-C parameter problems.

The results of the calculation stage, at the time points used in Fig. 5, are presented in Fig. 8a for the aortic case and in Fig. 8b for the CSF case. The mapped aortic profile retains both its inherent eccentricity and its steepness in the vicinity of the wall. In this case of increased cardiac output and large Reynolds number, the velocity profile is steeper than usually in the near wall region. The mapped analytical profiles of the Womersley solution cannot account for these characteristics sufficiently. The dissimilarity between the target polygonal domain, which does not deform, and the segmented moving aortic wall in the measurements

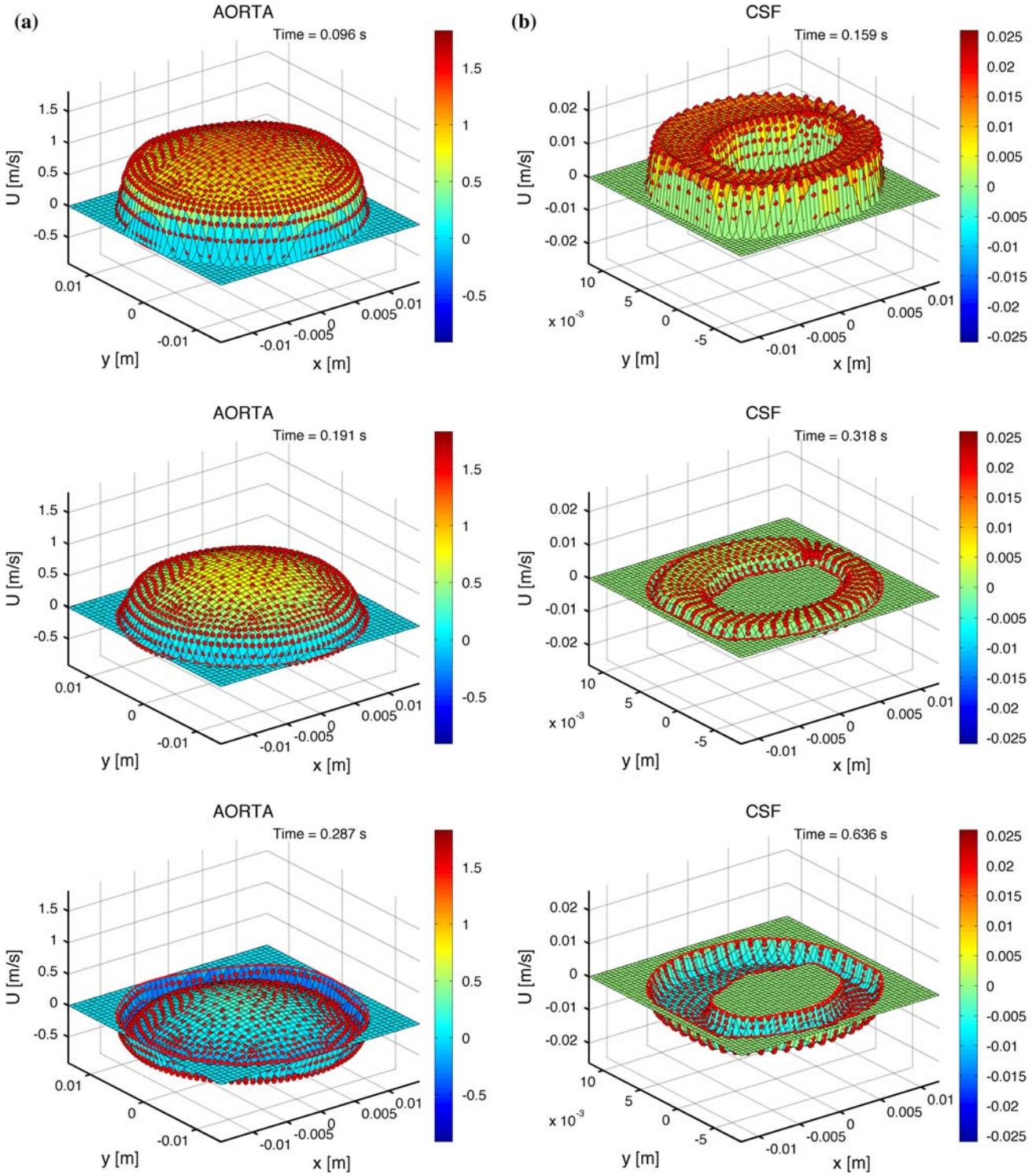

FIGURE 5. Mapped axisymmetric velocity profiles at three time-steps onto: (a) the aortic inlet and (b) the CSF inlet.

plane is a source of additional deformation and offset relative rotation. Nevertheless, these features do not alter the main characteristics of the mapped profile. Equally, the mapped profiles in the CSF case, Fig. 8b, appear to be different from their analytical counterparts. This is caused by the fact that the PC-MRI measurements show a radically different profile from the analytical solution, Fig. 4d. Furthermore, the significantly different inner polygonal contours between the target and the experimental cross-sections introduce

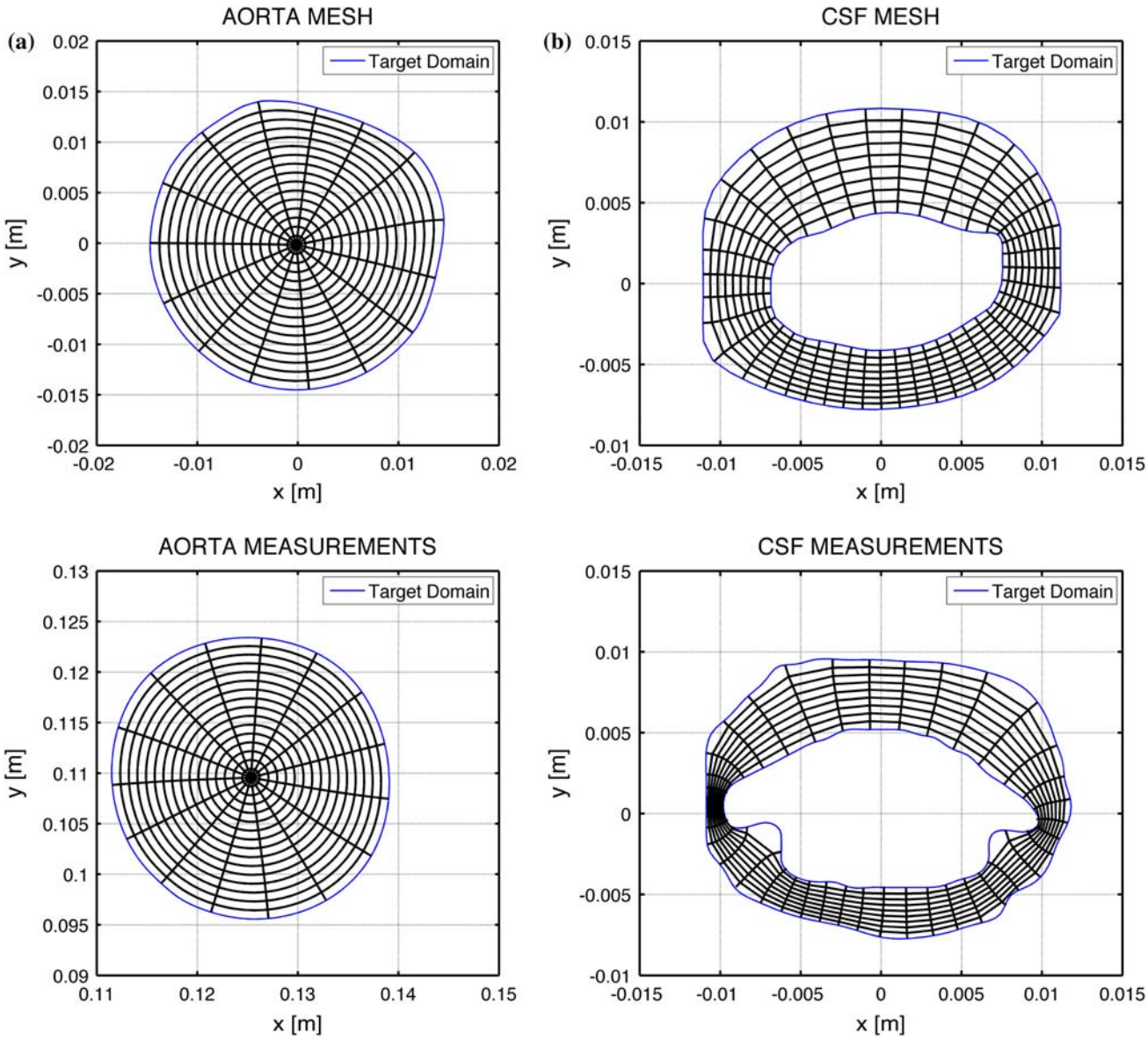

FIGURE 6. Illustration of the conformal mapping functions at the initial time-step: (a) f_1 and f_2 for the aortic case and (b) g_1 and g_2 for the CSF case.

deformation and offset rotation from the experimental velocity distribution in Fig. 7b. Hence, an angular correction in Eq. (14) should be considered. In all cases, the required velocity corrections fluctuated up to 10% of the mean instantaneous mapped velocity revealing the differences in the cross-sectional areas between the measurements and the computational domains.

DISCUSSION

A method for mapping analytical or experimentally determined velocity profiles on realistic boundary cross-sections has been outlined in the previous paragraphs. The interpolation algorithms are based on the S-C formulas for singly and doubly connected polygonal domains. The applicability of the technique was tested by producing velocity boundary conditions for CFD simulations of blood flow in the ascending aorta and CSF flow in the spinal cavity. On both occasions we created mappings of axisymmetric velocity profiles and interpolations from *in-vivo* PC-MRI velocity measurements with given instantaneous volumetric flux constraints. The target "inlet" surfaces remained stationary in all cases. Nevertheless, we had to take into account the lateral aortic motion in the measurement plane. Both mapped profiles provide appropriate

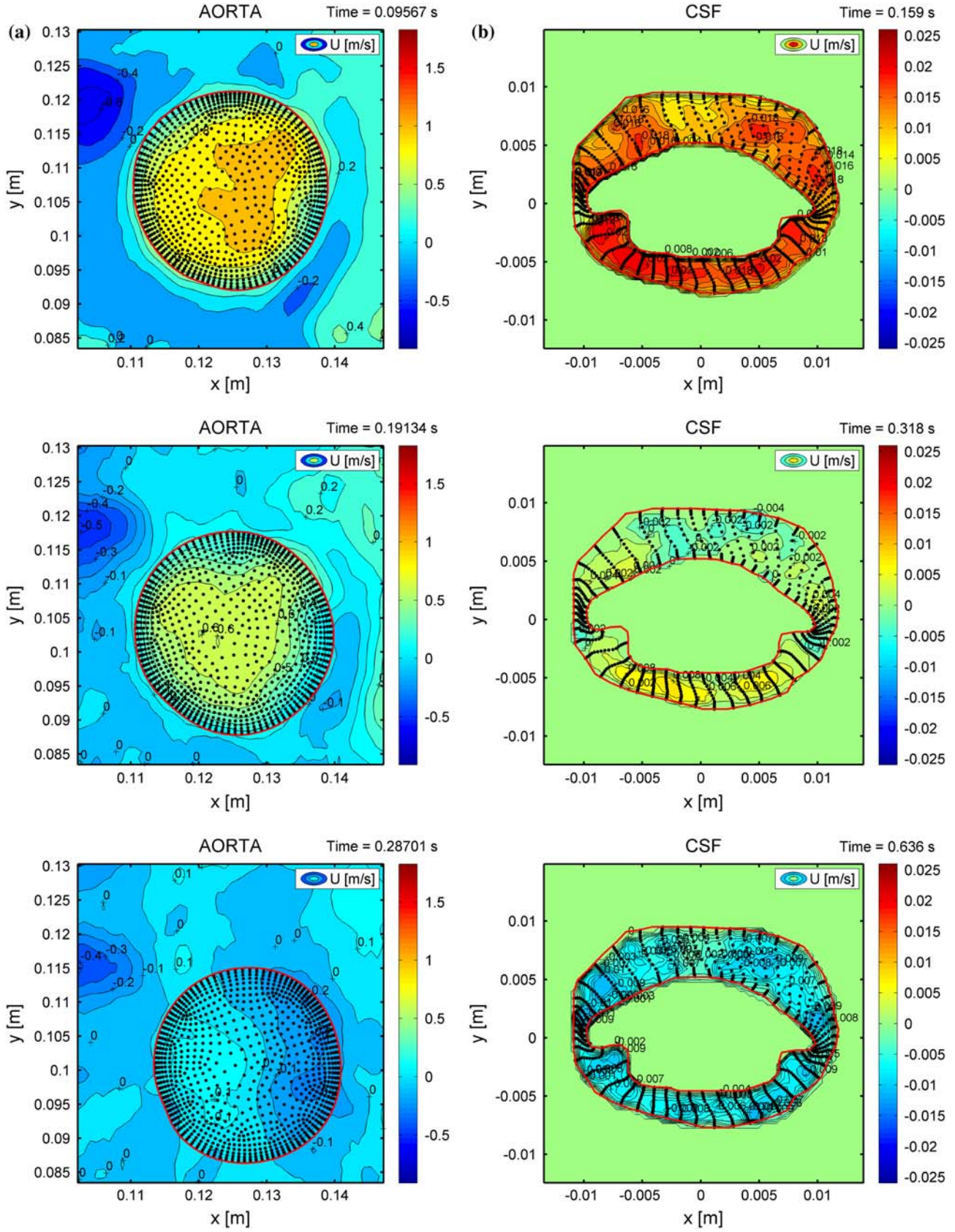

FIGURE 7. Three time instances of the interpolating surface fits, the bounding polygonal contours and the mapped faces centers in the measurements plane for: (a) the aortic case and (b) the CSF case.

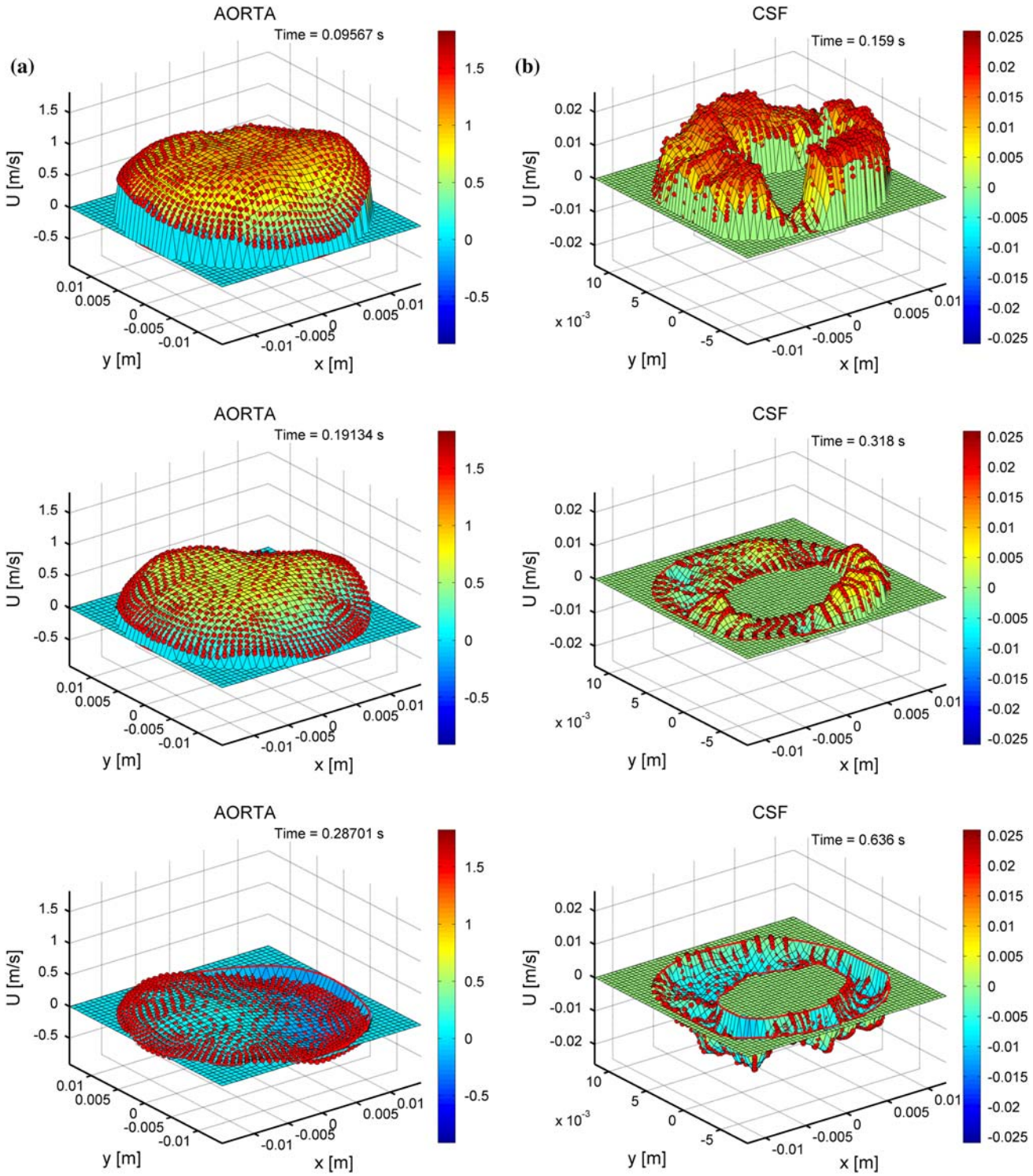

FIGURE 8. Mapped non-analytical velocity profiles at three time-steps onto: (a) the aortic inlet and (b) the CSF inlet.

velocity boundary conditions for CFD applications. The experimental mappings contain more physiological characteristics, like eccentricity in the aortic case, whereas the analytical maps are smoother and easier to implement. *In-vivo* CSF MRI measurements are often noisy and of insufficient resolution. Therefore, this technique provides us with a viable alternative. We will enhance the presented method to include the analytical solution of oscillatory flow through elliptic annular domains and the S-C map between a canonical elliptic

annulus to a doubly connected bounded polygon. Apparently, this is a closer match to the realistic CSF boundary cross-sections.

The S-C transformations facilitate the construction of a one-to-one invertible correlation between the boundary target surface and an arbitrary closed domain. We may then build an interpolating function within the measurement plane without making any provisions for the shape of the target boundary cross-section. Alternatively, one should overlap the two non-matching spaces, a process susceptible to errors leading to erroneous inclusion or exclusion of data. The proposed technique permits us to segment each space separately and map one onto the other in its entirety. Another advantage arises from the fact that a conformal map preserves local angles. This property becomes important when considering applications where the computational domain moves and/or deforms. Apart from providing the means to deform the internal boundary grid when the motion of the surrounding contour is given, this technique ensures that the angular quality will not degrade. We intend to expand on this aspect in future work.

Nonetheless, there are points that necessitate caution. The volumetric flux is not conserved intrinsically when transferring an analytical profile or mapping from a measurement domain. It is possible to scale the reference domain by equating its cross-sectional area to the corresponding values of the target boundary surface. When the volumetric flux is given, this is the only way to maintain the same Reynolds and Womersley numbers between the two spaces. In the latter case, there are no fine-tuning options. The discrepancy in the acquired volumetric flux depends on shape and area differences between the measurements plane and the targeted boundary cross-section. A velocity correction proportional to these differences is needed. Apart from the preservation of volumetric flux, additional constraints may be proposed such as the conservation of kinetic energy or of spatial moments between the original and the mapped velocity profiles. In this first attempt, the presented study did not address these issues. A possible solution is to incorporate such constraints in the construction of the S-C mapping functions themselves by quantifying shape differences between the source and target polygons.

Continuity is one more property that is not conserved *per se* when mapping from an analytical or experimental incompressible viscous flow field. In the presented examples, the velocity field had a single non-zero normal component. Hence, the issue of incompressibility is not raised. If the technique is used to project the tangential velocity components as well, continuity will be violated within the target polygonal domain. This is not true only within the limits of potential flow theory. Another complication is the possibility of relative rotation between the target boundary surface and the measurements plane. The substance of this technique is the interpolation between the images of the respective spaces within the same or similar canonical domains. In both cases, we presumed that these images are aligned and therefore we did not apply any angular corrections. This hypothesis is based on the fact that similar polygons will produce similar images in the canonical domains. However, this is not true in cases when the two target polygons are very different in shape and geometrical proportions and/or have a very different number of vertices. The CSF case provided such an example where the introduction of an angular correction in the canonical space should be considered.

In conclusion, the presented method is computationally inexpensive as far as the investigated examples are concerned. The surrounding polygons possessed a moderate number of nodes, 100 or less. Both DSC-PACK and the S-C MATLAB Toolbox are inefficient when dealing with polygons of a larger number of vertices. An important improvement is presented in the study of Banjai and Trefethen,[1] which proposes a multipole method for S-C mapping of singly connected polygons with thousands of sides. Our investigation was focused on computational hemodynamics. However, this technique can be used for the mapping of any scalar or vector variable. Conformal mapping and the S-C transform in particular is an accurate, elegant, but also sophisticated mathematical tool and an overall adoption of this technique cannot be suggested just yet. In a follow up study, it would be interesting to test the several existing techniques on a common set of geometry and velocity data in order to quantify algorithmic complexity, calculation times and accuracy of each method on equal grounds. We believe that the presented interpolation method shall prove particularly helpful in the imposition of boundary conditions.

APPENDIX

Tsangaris[26] has given the axisymmetric Navier–Stokes solution for fully developed oscillatory flow through an annular pipe. The flow is driven by a harmonic pressure gradient along the pipe's length with a non-zero mean value and frequency ω. Let the axial pressure gradient and corresponding velocity be defined by Eq. (17).

$$\begin{cases} \frac{\partial P}{\partial x}(t) = P_x^{\mathrm{c}} + P_x^{\mathrm{osc}} \cdot e^{i\omega t} \\ u(r,t) = u_{\mathrm{s}}(r) + \mathrm{Real}\left\{ \underbrace{u_{\mathrm{osc}}(r) \cdot e^{i\omega t}}_{u_{\mathrm{osc}}(r,t)} \right\}, \end{cases} r \in \left[R_{\mathrm{eqi}}, R_{\mathrm{eqo}}\right], \tag{17}$$

where, P_x^{c} is a constant denoting the mean value of the pressure oscillation and P_x^{osc} its amplitude. The velocity consists of a steady part, $u_{\mathrm{s}}(r)$, and an oscillating part with complex amplitude, $u_{\mathrm{osc}}(r)$, shown in Eqs. (18) and (19), respectively.

$$u_{\mathrm{s}}(r) = \frac{P_x^{\mathrm{c}}}{4\mu} \cdot \left[R_{\mathrm{eqo}}^2 - r^2 + \left(R_{\mathrm{eqo}}^2 - R_{\mathrm{eqi}}^2\right) \frac{\ln\left(r/R_{\mathrm{eqo}}\right)}{\ln\left(R_{\mathrm{eqo}}/R_{\mathrm{eqi}}\right)} \right], \quad r \in \left[R_{\mathrm{eqi}}, R_{\mathrm{eqo}}\right] \tag{18}$$

$$u_{\mathrm{osc}}(r) = \frac{P_x^{\mathrm{osc}}}{i\rho\omega} \cdot \left[k_1 \cdot K_0(\xi) + k_2 \cdot I_0(\xi) - 1\right] \quad \text{with } \xi = i^{1/2} \cdot \sqrt{\frac{\omega}{\nu}} \cdot r \text{ and } r \in \left[R_{\mathrm{eqi}}, R_{\mathrm{eqo}}\right], \tag{19}$$

where, ρ is the fluid's density and μ and ν the dynamic and kinematic viscosity. I_0 and K_0 are the zeroth order modified Bessel functions of the first and second kind. The coefficients k_1 and k_2 are given below.

$$k_1 = \frac{\left[\frac{1}{I_0(\xi_0)} - \frac{1}{I_0(\xi_i)}\right]}{\left[\frac{K_0(\xi_0)}{I_0(\xi_0)} - \frac{K_0(\xi_i)}{I_0(\xi_i)}\right]} \text{ and } k_2 = \left[\frac{1}{I_0(\xi_0)} - \frac{K_0(\xi_0)}{I_0(\xi_0)} \cdot k_1\right] \quad \text{with } \xi_0 = i^{1/2} \cdot \sqrt{\frac{\omega}{\nu}} \cdot R_{\mathrm{eqo}} \text{ and } \xi_i = i^{1/2} \cdot \sqrt{\frac{\omega}{\nu}} \cdot R_{\mathrm{eqi}} \tag{20}$$

The instantaneous volumetric flow rate can be obtained by integrating the velocity field over the annular cross-sectional area and in turn consists of two components.

$$\dot{Q}(t) = \dot{Q}_{\mathrm{s}} + \mathrm{Real}\left\{\dot{Q}_{\mathrm{osc}}(t)\right\} = 2\pi \int_{R_{\mathrm{eqi}}}^{R_{\mathrm{eqo}}} u_{\mathrm{s}}(r) \cdot r \cdot dr + \mathrm{Real}\left\{ 2\pi \int_{R_{\mathrm{eqi}}}^{R_{\mathrm{eqo}}} \left(u_{\mathrm{osc}}(r) \cdot e^{i\omega t}\right) \cdot r \cdot dr \right\}, \tag{21}$$

$$\dot{Q}_{\mathrm{s}} = \frac{P_x^{\mathrm{c}}}{8\mu} \cdot \underbrace{\pi \cdot \left(R_{\mathrm{eqo}}^2 - R_{\mathrm{eqi}}^2\right) \cdot \left[R_{\mathrm{eqo}}^2 + R_{\mathrm{eqi}}^2 - \frac{\left(R_{\mathrm{eqo}}^2 - R_{\mathrm{eqi}}^2\right)}{\ln\left(R_{\mathrm{eqo}}/R_{\mathrm{eqi}}\right)} \right]}_{k_4}, \tag{22}$$

$$\dot{Q}_{\mathrm{osc}}(t) = \frac{2\pi}{i\rho\omega} \cdot \left(P_x^{\mathrm{osc}} e^{i\omega t}\right) \cdot k_3 \text{ where } k_3 = \sqrt{\frac{\nu}{i\omega}} \cdot \begin{Bmatrix} k_1 \cdot \left[R_{\mathrm{eqi}} \cdot K_1(\xi_i) - R_{\mathrm{eqo}} \cdot K_1(\xi_0)\right] + \\ k_2 \cdot \left[R_{\mathrm{eqo}} \cdot I_1(\xi_0) - R_{\mathrm{eqi}} \cdot I_1(\xi_i)\right] - \\ \frac{R_{\mathrm{eqo}}^2 - R_{\mathrm{eqi}}^2}{2} \end{Bmatrix}, \tag{23}$$

where, I_1 and K_1 are the first order modified Bessel functions of the first and the second kind. By eliminating the pressure gradient from the previous equations we can express the instantaneous axisymmetric velocity as a function of the instantaneous volumetric flux.

$$u_{\mathrm{s}}(r) = \frac{2 \cdot \dot{Q}_{\mathrm{s}}}{k_4} \cdot \left[R_{\mathrm{eqo}}^2 - r^2 + \left(R_{\mathrm{eqo}}^2 - R_{\mathrm{eqi}}^2\right) \frac{\ln\left(r/R_{\mathrm{eqo}}\right)}{\ln\left(R_{\mathrm{eqo}}/R_{\mathrm{eqi}}\right)} \right], \quad r \in \left[R_{\mathrm{eqi}}, R_{\mathrm{eqo}}\right] \tag{24}$$

$$u_{\mathrm{osc}}(r,t) = \mathrm{Real}\left\{ \frac{\dot{Q}_{\mathrm{osc}}(t)}{2\pi} \cdot \left[\frac{k_1 \cdot K_0(\xi) + k_2 \cdot I_0(\xi) - 1}{k_3} \right] \right\}, \quad r \in \left[R_{\mathrm{eqi}}, R_{\mathrm{eqo}}\right] \tag{25}$$

Finally, the solution given by Eqs. (24) and (25) can be readily generalized to the case where the instantaneous flux has more than one harmonics and is given by a Fourier series.

$$\dot{Q}(t) \approx \sum_{n=0}^{N} B_n \cdot e^{\mathrm{in}\omega t} \tag{26}$$

Then the axisymmetric velocity field is given by the following formula for $r \in [R_{\mathrm{eqi}}, R_{\mathrm{eqo}}]$:

$$u(r,t) = \frac{2B_0}{k_4} \cdot \left[R_{\mathrm{eqo}}^2 - r^2 + \left(R_{\mathrm{eqo}}^2 - R_{\mathrm{eqi}}^2\right) \cdot \frac{\ln\left(r/R_{\mathrm{eqo}}\right)}{\ln\left(R_{\mathrm{eqo}}/R_{\mathrm{eqi}}\right)} \right] + \mathrm{Real}\left\{ \sum_{n=1}^{N} \left[\frac{B_n}{2\pi} \cdot \frac{\left(k_{1n} \cdot K_0\left(i^{1/2} \cdot \sqrt{\frac{n\omega}{\nu}} \cdot r\right) + k_{2n} \cdot I_0\left(i^{1/2} \cdot \sqrt{\frac{n\omega}{\nu}} \cdot r\right) - 1\right)}{k_{3n}} \right] \cdot e^{\mathrm{in}\omega t} \right\}, \tag{27}$$

the coefficients k_{1n}, k_{2n} and k_{3n} are derived from the formulas for k_1, k_2 and k_3 by substituting ω with $n \cdot \omega$ for each frequency.

ACKNOWLEDGMENTS

This study was carried out within the "Computer Aided and Image Guided Medical Interventions" (CO-ME) program of the Swiss National Science Foundation (SNSF). The authors gratefully acknowledge the contribution of the aortic MRI velocimetry data by Professor Renè Prêtre and his group, Dr. med. Hitendu Dave and Dr. med. Emanuela Valsangiacomo, at Zurich Children's University Hospital. Additionally, we thank Michaela Soellinger from the Institute for Biomedical Engineering of ETH Zurich and University of Zurich for providing us with CSF MRI velocity measurements in the spinal cavity. Finally, Dr. Yiannis Ventikos, Reader in Engineering Science at the University of Oxford, is acknowledged for several helpful discussions.

REFERENCES

[1]Banjai, L., and L. N. Trefethen. A multipole method for Schwarz-Christoffel mapping of polygons with thousands of sides. *SIAM J. Sci. Comput*. 25:1042–1065, 2003. doi:10.1137/S1064827502411675.

[2]Blanco, P. J., R. A. Feijoo, and S. A. Urquiza. A unified variational approach for coupling 3D-1D models and its blood flow applications. *Comput. Meth. Appl. Mech. Eng*. 196:4391–4410, 2007. doi:10.1016/j.cma.2007.05.008.

[3]Boutsianis, E., H. Dave, T. Frauenfelder, D. Poulikakos, S. Wildermuth, M. Turina, Y. Ventikos, and G. Zund. Computational simulation of intracoronary flow based on real coronary geometry. *Eur. J. Cardio-Thorac*. 26:248–256, 2004. doi:10.1016/j.ejcts.2004.02.041.

[4]Di Martino, E. S., G. Guadagni, A. Fumero, G. Ballerini, R. Spirito, P. Biglioli, and A. Redaelli. Fluid–structure interaction within realistic three-dimensional models of the aneurysmatic aorta as a guidance to assess the risk of rupture of the aneurysm. *Med. Eng. Phys*. 23:647–655, 2001. doi:10.1016/S1350-4533(01)00093-5.

[5]Driscoll, T. A. Algorithm 756: a MATLAB toolbox for Schwarz-Christoffel mapping. *ACM T. Math. Software* 22:168–186, 1996. doi:10.1145/229473.229475.

[6]Driscoll, T. A. Algorithm 843: improvements to the Schwarz-Christoffel toolbox for MATLAB. *ACM T. Math. Software* 31:239–251, 2005. doi:10.1145/1067967.1067971.

[7]Driscoll, T. A. and L. N. Trefethen. Schwarz-Christoffel Mapping. Cambridge: Cambridge University Press, 132 pp, 2002.

[8]Giddens, D. P., C. K. Zarins, and S. Glagov. The role of fluid-mechanics in the localization and detection of atherosclerosis. *J. Biomech. Eng*. 115:588–594, 1993.

[9]Heywood, J. G., R. Rannacher, and S. Turek. Artificial boundaries and flux and pressure conditions for the incompressible Navier–Stokes equations. *Int. J. Numer. Methods Fluids* 22:325–352, 1996. doi:10.1002/(SICI)1097-0363(19960315)22:5<325::AID-FLD307>3.0.CO;2-Y.

[10]Hu, C. L. Algorithm 785: a software package for computing Schwarz-Christoffel conformal transformation for doubly connected polygonal regions. *ACM T. Math. Software* 24:317–333, 1998. doi:10.1145/292395.291204.

[11]Jin, S., J. Oshinski, and D. P. Giddens. Effects of wall motion and compliance on flow patterns in the ascending aorta. *J. Biomech. Eng*. 125:347–354, 2003. doi:10.1115/1.1574332.

[12]Kern, M. J. Curriculum in interventional cardiology: coronary pressure and flow measurements in the cardiac Catheterization laboratory. *Catheter. Cardiovasc. Interv*. 54:378–400, 2001. doi:10.1002/ccd.1303.

[13]Kurtcuoglu, V., M. Soellinger, P. Summers, K. Boomsma, D. Poulikakos, P. Boesiger, and Y. Ventikos. Reconstruction of cerebrospinal fluid flow in the third ventricle based on MRI data. *Lect. Notes Comput. Sci*. 3749:786–793, 2005.

[14]Li, Z. H., and C. Kleinstreuer. Blood flow and structure interactions in a stented abdominal aortic aneurysm model. *Med. Eng. Phys*. 27:369–382, 2005. doi:10.1016/j.medengphy.2004.12.003.

[15]Lotz, J., C. Meier, A. Leppert, and M. Galanski. Cardiovascular flow measurement with phase-contrast MR imaging: basic facts and implementation. *Radiographics* 22:651–671, 2002.

[16]Migliavacca, F., R. Balossino, G. Pennati, G. Dubini, T. Y. Hsia, M. R. de Leval, and E. L. Bove. Multiscale modelling in biofluidynamics: application to reconstructive paediatric cardiac surgery. *J. Biomech*. 39:1010–1020, 2006. doi:10.1016/j.jbiomech.2005.02.021.

[17]Moyle, K. R., L. Antiga, and D. A. Steinman. Inlet conditions for image-based CFD models of the carotid bifurcation: is it reasonable to assume fully developed flow? *J. Biomech. Eng*. 128:371–379, 2006. doi:10.1115/1.2187035.

[18]Perktold, K., M. Hofer, G. Rappitsch, M. Loew, B. D. Kuban, and M. H. Friedman. Validated computation of physiologic flow in a realistic coronary artery branch. *J. Biomech*. 31:217–228, 1998. doi:10.1016/S0021-9290(97)00118-8.

[19]Quarteroni, A., and A. Veneziani. Analysis of a geometrical multiscale model based on the coupling of ODEs and PDEs for blood flow simulations. *Multiscale Model. Simul*. 1:173–195, 2003. doi:10.1137/S1540345902408482.

[20]Ramaswamy, S. D., S. C. Vigmostad, A. Wahle, Y. G. Lai, M. E. Olszewski, K. C. Braddy, T. M. H. Brennan, J. D. Rossen, M. Sonka, and K. B. Chandran. Fluid dynamic analysis in a human left anterior descending coronary artery with arterial motion. *Ann. Biomed. Eng*. 32:1628–1641, 2004. doi:10.1007/s10439-004-7816-3.

[21]Redaelli, A., F. Boschetti, and F. Inzoli. The assignment of velocity profiles in finite element simulations of pulsatile flow in arteries. *Comput. Biol. Med*. 27:233–247, 1997. doi:10.1016/S0010-4825(97)00006-1.

[22]Shahcheraghi, N., H. A. Dwyer, A. Y. Cheer, A. I. Barakat, and T. Rutaganira. Unsteady and three-dimensional simulation of blood flow in the human aortic arch. *J. Biomech. Eng*. 124:378–387, 2002. doi:10.1115/1.1487357.

[23]Taylor, C. A., and M. T. Draney. Experimental and computational methods in cardiovascular fluid mechanics. *Annu. Rev. Fluid Mech*. 36:197–231, 2004. doi:10.1146/annurev.fluid.36.050802.121944.

[24]Taylor, C. A., T. J. R. Hughes, and C. K. Zarins. Finite element modeling of three-dimensional pulsatile flow in the abdominal aorta: relevance to atherosclerosis. *Ann. Biomed. Eng*. 26:975–987, 1998. doi:10.1114/1.140.

[25]Trefethen, L. N. Numerical computation of the Schwarz-Christoffel transformation. *SIAM J. Sci. Stat. Comp.* 1:82–102, 1980. doi:10.1137/0901004.
[26]Tsangaris, S. Oscillatory flow of an incompressible, viscous-fluid in a straight annular pipe. *J. Mec. Theor. Appl.* 3:467–478, 1984.
[27]Tsangaris, S., and N. Stergiopulos. The inverse Womersley problem for pulsatile flow in straight rigid tubes. *J. Biomech.* 21:263–266, 1988. doi:10.1016/0021-9290(88)90176-5.
[28]Wolters, B. J. B. M., M. C. M. Rutten, G. W. H. Schurink, U. Kose, J. de Hart, and F. N. van de Vosse. A patient-specific computational model of fluid–structure interaction in abdominal aortic aneurysms. *Med. Eng. Phys.* 27:871–883, 2005. doi:10.1016/j.medengphy.2005.06.008.
[29]Womersley, J. R. Method for the calculation of velocity, rate of flow and viscous drag in arteries when the pressure gradient is known. *J. Physiol. Lond.* 127:553–563, 1955.
[30]Zamir, M. The Physics of Pulsatile Flow. New York: Springer, 220 pp, 2000.
[31]Zeng, D. H., Z. H. Ding, M. H. Friedman, and C. R. Ethier. Effects of cardiac motion on right coronary artery hemodynamics. *Ann. Biomed. Eng.* 31:420–429, 2003. doi:10.1114/1.1560631.